

# Generation of Schrödinger's cat states in a planar semiconductor heterostructure

J. Pawłowski, M. Górski, G. Skowron, and S. Bednarek

*Faculty of Physics and Applied Computer Science,  
AGH University of Science and Technology, Kraków, Poland*

(Dated: May 21, 2022)

We propose a nanodevice based on a typical planar semiconductor heterostructure with lateral confinement potential created by voltages applied to local electrodes. We show how to obtain near parabolical confinement along the nanodevice, and how to use coherent states of the harmonic oscillator for spatial separation of electron densities corresponding to opposite spin directions. In such a way, an entangled state of Schrödinger's cat type is created. We performed simulations of a realistic nanodevice model by numerical solving the time-dependent Schrödinger's equation together with simultaneous tracking of the controllable confinement potential via solution of the Poisson's equation at every time step.

## I. INTRODUCTION

Control and manipulation of single electrons trapped in semiconductor nanostructures attract much attention due to potential applications in spintronics<sup>1,2</sup> or quantum computing<sup>3</sup>. This enables us to examine numerous fundamental physical phenomena and discover a new physics, e.g. topological effects<sup>4,5</sup> or exotic quasiparticles<sup>6–9</sup>.

An electron qubit can be represented in many different ways<sup>10</sup>. In the case of a charge qubit<sup>11–13</sup>, two basis states are defined as the presence of an electron on one of two sides of a double quantum dot or wire structure. However, the spin degree of freedom will probably be used as a bit carrier in the quantum computer, i.e. spin qubit<sup>14,15</sup>. This explains the necessity for precise electron control to perform operations on qubits, or to couple them into registers<sup>16–22</sup>, and transmit information between individual registers of the quantum computer<sup>23–26</sup>. Spin-orbit interaction of Rashba type (RSOI)<sup>27–29</sup>, which couples the orbital and spin degrees of freedom of an electron, allows for effective manipulation of a spin qubit<sup>30–39</sup>.

An important issue in quantum computing is the generation of entangled states. The Schrödinger's cat state is a notable example<sup>40–43</sup>. This has been successfully generated in quantum optics using coherent states<sup>44–48</sup>. The possibility to create coherent states has also been examined in solid-state systems<sup>10,49,50</sup>. However, creation of their combination with opposite spin, namely the Schrödinger's cat state, poses a great challenge due to its high instability<sup>40,46,51,52</sup>.

In this paper, we propose to repeat these quantum optics experiments in a solid state system. We show the possibility for the creation of a Schrödinger's cat state in a typical and easily obtainable semiconductor heterostructure. This is the method extension, introduced in [50], here developed on heterostructures which are much more easily scalable. Control over an electron is achieved all electrically by applying voltages to local device electrodes. The spin separation of coherent states, forming in superposition the Schrödinger's cat state, is achieved

with an electrically controlled Rashba spin-orbit coupling in the nanostructure.

The paper is organized as follows. In the first part (Sec. II) of the article we employ a one-dimensional (1D) approximation with modeled potentials and the method for the generation of the Schrödinger's cat state is discussed only qualitatively. In the latter part (Sec. III) we propose a nanodevice based on a planar semiconductor heterostructure. The design includes geometrical details and parameters for the materials used, for which we assume realistic values. Potentials are calculated using the Poisson's equation with all important effects included. The results from this part are quantitative in nature.

## II. EXPLAINING THE EFFECT WITH A SIMPLIFIED MODEL

### A. Simplified one-dimensional model

The Hamiltonian of a single electron trapped in a quantum wire—a 1D structure—oriented along the  $x$ -axis has the following form:

$$H(x, t) = -\frac{\hbar^2}{2m} \frac{\partial^2}{\partial x^2} + V(x) + H_{\text{so}}(t), \quad (1)$$

where  $V(x)$  constitutes the potential energy of an additional confinement along the wire and  $H_{\text{so}}(t)$  describes the spin-orbit interaction (SOI)<sup>27–29</sup>. If the quantum wire axis is parallel to the crystallographic direction [111], the Dresselhaus interaction becomes negligible<sup>29,32</sup>. Now if we apply an electric field along the  $y$ -axis, an RSOI is introduced. It can be described by the following Hamiltonian:

$$H_{\text{so}}(t) = -\frac{\alpha_{\text{so}}|e|}{\hbar} E_y(t) \hat{p}_x \sigma_z, \quad (2)$$

with the material RSOI coefficient  $\alpha_{\text{so}}$ , the electric field  $E_y(t)$  (perpendicular to the wire direction), the Pauli  $z$ -matrix  $\sigma_z$ , and the electron momentum operator  $\hat{p}_x$ .

If the confinement potential along the wire has a parabolic shape  $V(x) = m\omega^2 x^2/2$ , we can solve the

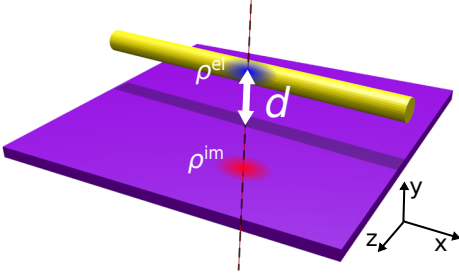


FIG. 1. Scheme depicting the simplified 1D model with a quantum wire above a conducting plate at distance  $d$ .

eigenequation of this Hamiltonian analytically in the momentum representation and then return to the position representation<sup>50</sup>. The energy of the ground state is doubly degenerated with respect to spin values. The ground state wavefunction in the position representation takes the form of a Gaussian multiplied by a plane wave. Depending on the spin  $z$ -projection its wavenumber is either positive or negative. The two basis functions corresponding to the ground state have the form:

$$\Psi_{\uparrow}(x) = \left(\frac{2\beta}{\pi}\right)^{\frac{1}{4}} \begin{pmatrix} 1 \\ 0 \end{pmatrix} e^{-\beta x^2} e^{iqx}, \quad (3)$$

$$\Psi_{\downarrow}(x) = \left(\frac{2\beta}{\pi}\right)^{\frac{1}{4}} \begin{pmatrix} 0 \\ 1 \end{pmatrix} e^{-\beta x^2} e^{-iqx}, \quad (4)$$

with  $\beta = \frac{m\omega}{2\hbar}$  and the wavenumber  $q = \frac{m\alpha_{so}eE_y(t=0)}{\hbar^2}$ .

We should note that the wavenumber  $q$  does not depend on the harmonic potential curvature (frequency  $\omega/2\pi$ ). Due to the degeneration, any linear combination of both basis states corresponds to the same energy. The SOI merely introduces an energy correction  $\Delta E = \frac{\hbar^2 q^2}{2m}$ .

### B. Semiconductor electron soliton – an inducton

We assume that the quantum wire is aligned in parallel to a metallic electrode, as shown in Fig. 1. If we trap an electron inside the wire, an opposite charge will be induced on the surface of the conductor. This induced charge attracts the electron and causes the electric field to have a component directed toward the center of the electron density resulting in a self-focusing of the electron wavefunction. Thus, an electron soliton called an inducton<sup>53</sup> is formed. The electron becomes trapped under the electrode, creating a stable Gaussian-like wavepacket of finite size, capable of moving without changing its shape. Therefore, the electron exhibits properties unusual for a quantum object<sup>53,54</sup>. In the quantum regime, the electron density usually partially reflects off an obstacle and partially tunnels through it. However, due to self-focusing, the wavepacket does not divide and

shows a classical-like behavior. Similar to a classical particle, it either reflects off obstacles or tunnels through them with 100% probability<sup>54</sup>. Because of such localization we can relocate the electron within the wire in a controllable manner<sup>23,24,55</sup>. Moreover, inductons and their spins can be used as quantum bit carriers in the quantum computer<sup>22,24,53,55</sup>.

If the electrode is an infinite conducting plate, the potential created by the induced charge can be described using the image charge method. The induced charge is replaced by an image charge which is a reflection (against the surface of the conductor) of the primary charge density from the quantum wire<sup>54</sup>. For a quantum wire placed at distance  $d$  from the conducting plate, the potential energy created by interaction with the image charge can be expressed in the following way:

$$U^{\text{ind}}(x) = \frac{-|e|}{4\pi\epsilon\epsilon_0} \int \frac{\rho^{\text{im}}(x')}{\sqrt{(x-x')^2 + 4d^2}} dx', \quad (5)$$

with the image charge density  $\rho^{\text{im}}(x)$  being a mirrored version of the electron charge from the quantum wire  $\rho^{\text{el}}(x)$ —see Fig. 1, and calculated as

$$\rho^{\text{im}}(x) = -\rho^{\text{el}}(x) = |e||\Psi(x)|^2. \quad (6)$$

If there is no additional external potential in (Eq. 1), only the interaction energy with the image charge is present:  $V(x) = U^{\text{ind}}(x)$ . Since the image charge method is applicable only for cases of an infinite interface between a dielectric medium and a metallic plate, this approach is used only for model potentials in the first part of this article (Sec. II). For actual realizations of the nanodevice (Sec. III), the potential inside the quantum wire is exactly calculated using the Poisson's equation. This method is slightly more complex; however, it guarantees correct inclusion of the induced charge on electrodes of any shape or dimension<sup>56</sup>.

The potential energy originating from the induced charge present on the electrode parallel to the quantum wire takes an approximately parabolic shape<sup>53</sup>. Therefore, if this potential energy, and the SOI generated by the electric field are taken into account, the wavefunction of the electron ground state in the wire is a Gaussian multiplied by a plane wave as in (Eq. 3, 4).

### C. Control of the electron motion

Let us assume that the electron spin is directed along the  $z$ -axis (spin  $z$ -projection  $s_z = \hbar/2$ ) with a nonzero electric field  $E_y$ . In such a case the ground state wavefunction assumes the form of (Eq. 3). This is a stationary state and the wavepacket remains fixed even though the wavefunction is a Gaussian multiplied by a plane wave. This happens because motion is blocked by the SOI included in the Hamiltonian. However, if we disable the electric field abruptly<sup>57,58</sup>, inserting  $E_y = 0$ , the SOI disappears and the electron starts moving in the  $x$ -direction.

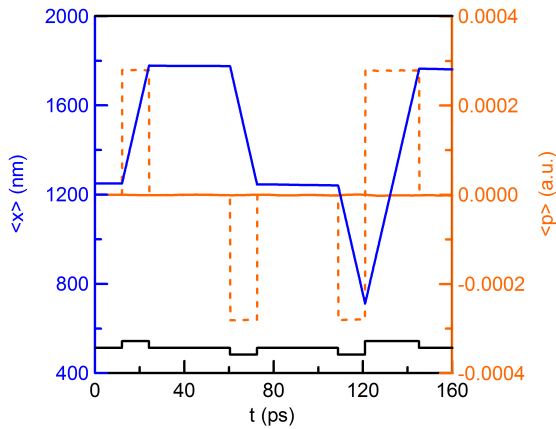


FIG. 2. Simulation of the electron motion induced by changes of the electric field perpendicular to the quantum wire. The black curve denotes the  $E_y(t)$  value, the blue curve—position of the electron, the solid red curve—expectation value the electron momentum and the dashed red one—classical momentum calculated as a time derivative of the position multiplied by the electron mass.

Setting  $E_y$  back to the previous value stabilizes the electron again, while using a greater value for  $E_y$  forces movement in the opposite direction. Thus, we gain a method to control the electron motion using an electric field perpendicular to the direction of motion.

Now we assume that the ground state is generated with  $E_y = 0$ . This time the wavefunction is again a Gaussian but no longer multiplied by a plane wave. We propel the electron by setting non-zero  $E_y$ . Fig. 2 shows an electron motion induced by changes of the electric field. The black curve denotes the value of  $E_y$ , the blue curve denotes the expectation value of position, the solid red one denotes the expectation value of momentum and the dashed red one denotes the classical momentum calculated as a time derivative of the position multiplied by the electron mass. Initially, we apply no electric field ( $E_y = 0$ ) and the electron remains stable. At  $t = 10$  ps we set a positive value for  $E_y$ , which sets the electron in motion in the direction of positive values of  $x$ . At  $t = 20$  ps, we set the electric field back to zero and the electron halts. Finally at  $t = 60$  ps, the electric field is set to  $-E_y$ , which induces movement toward negative values of  $x$ . Further manipulation of the electric field alters the velocity and the direction of the electron motion. We should notice that, despite the movement occurring at various velocities (corresponding to different values of the classical momentum), the expectation value of momentum operator remains zero, which means that the wavefunction is only a Gaussian, yet not multiplied by a plane wave. However, if the electric field is non-zero (SOI present), this state is no longer stationary. Therefore, the electron motion is initiated as a result of the change of the Hamiltonian, and not the wavefunction.

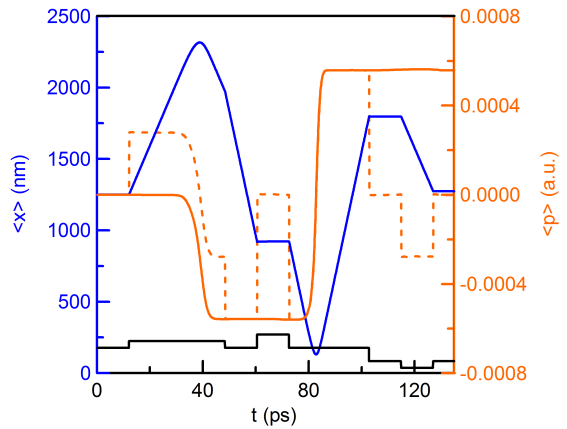


FIG. 3. Simulation of the electron motion including reflection off the walls at the wire ends. Markings as in Fig. 2.

The situation changes significantly if we allow the electron to reflect off the wall of the potential formed at the wire ends. In the Fig. 3, we can track the motion of the electron in such a case with reflections occurring at  $t = 40$  ps and  $t = 83$  ps. After reflection, the electron moves with the same speed but in the opposite direction to the initial one. This indicates that the wavefunction has been effectively multiplied by a plane wave with a doubled wavenumber  $2q$ . The expectation value of the momentum operator is no longer zero, but still inconsistent with the classical momentum. At the moment  $t = 120$  ps, the directions of both these quantities are actually opposite to each other.

#### D. Accelerating the electron – a synchrotron

The change of the wavefunction due to reflection can be exploited for wavepacket acceleration. In Fig. 4 we see a simulation of the electron motion induced in a rectangular potential well by square pulses of the electric field. The pulses have constant amplitude and duration carefully tuned to the moment of transition of the wavepacket through the central point of the wire. With every change of direction of the electric field, the electron is being accelerated. With increasing speed of the electron, the time between reflections decreases; hence, the changes of the electric field must be performed at decreasing periods of time.

This inconvenience can be mitigated by putting the electron in an external parabolic confinement potential. In this case, with no SOI, the ground state wavefunction of the electron assumes a Gaussian form:

$$\Psi(x) = \left(\frac{2\beta}{\pi}\right)^{\frac{1}{4}} e^{-\beta x^2}. \quad (7)$$

Multiplication of this Gaussian by a plane wave sets the

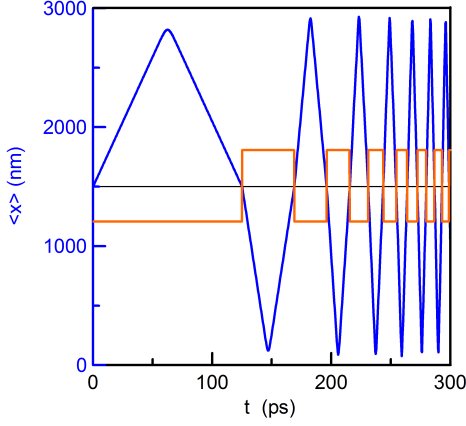


FIG. 4. Acceleration of the electron by square pulses of the electric field. The red curve denotes the value of the electric field  $E_y$  while the blue curve shows the expectation value of position of the electron wavepacket.

electron in an oscillatory motion with an amplitude dependent on  $q$ , yielding

$$\Psi(x) = \left(\frac{2\beta}{\pi}\right)^{\frac{1}{4}} e^{-\beta x^2} e^{iqx}. \quad (8)$$

Fig. 5 shows the motion of the electron initially set as the ground state of a harmonic oscillator, without SOI but multiplied by a plane wave with three different values for  $q$ . Regardless of the actual value of the wavenumber  $q$  (and energy) the periods of oscillations remain the same. This effect can be used for motion synchronization.

If the electron is confined in a harmonic potential with additional spin-orbit coupling, varying sinusoidally with frequency  $\omega/2\pi$  consistent with the frequency of

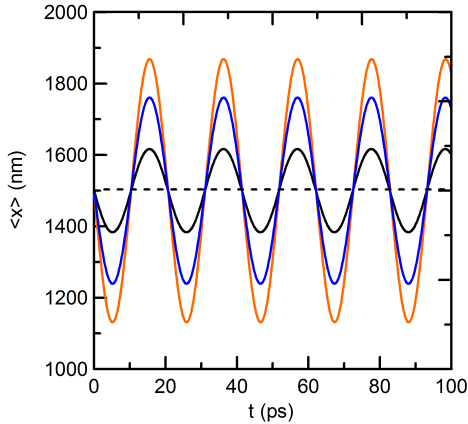


FIG. 5. Motion of the electron in an external parabolic potential calculated for three different values for the wavenumber  $q$  in (Eq. 8).

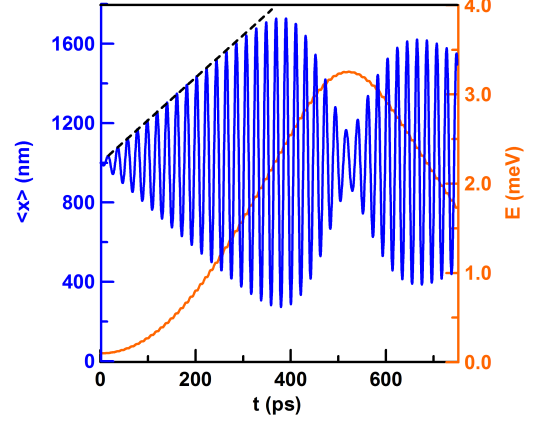


FIG. 6. Acceleration of the electron confined in a harmonic potential using a sinusoidally varying electric field  $E_y(t)$ . The blue line denotes the expectation value of position and the red one—the energy of the electron.

the harmonic potential, we can accelerate the electron to high velocities using only low electrode voltages (and thus we obtain a synchrotron-like device). This can be achieved using a sinusoidally oscillating electric field  $E_y(t) = E_0 \sin(\omega t)$  applied in the area occupied by the electron. The Fig. 6 shows the motion of the wavepacket subjected to such a field. In the time interval between  $t = 0$  ps and  $t = 300$  ps the expectation value of the position (blue curve) oscillates with a linearly increasing amplitude. The energy (red curve) rises quadratically in a step-wise manner, because the wavenumber rises by the same value with each oscillation of position.

An increase in the position oscillations amplitude, and hence also in energy, requires an exactly parabolic confinement potential. Non-parabolicity constitutes a natural limit to energy growth. In the simulation shown in Fig. 6, the wavepacket is confined in a parabolic potential but the calculations are performed on a finite fragment of the quantum wire which effectively imposes infinite potential walls at both ends of the wire. As the electron approaches the wire borders, the frequency of its oscillations is no longer consistent with the frequency of the time-varying electric field inducing its movement. The amplitude of spatial oscillations of the wavepacket ceases to grow. The influence of nonparabolicity is easily visible in Fig. 6 for  $t > 300$  ps.

In all the presented simulations we assumed that initially the electron spin is parallel to the  $z$ -axis. Despite the electron movement, the spin did not change, since according to the Hamiltonian (Eq. 2), movement along the  $x$ -axis implies rotation of spin around the  $z$ -axis. The situation would be similar if the initial spin was antiparallel to the  $z$ -axis. It would only result in an opposite direction for the electron movement.

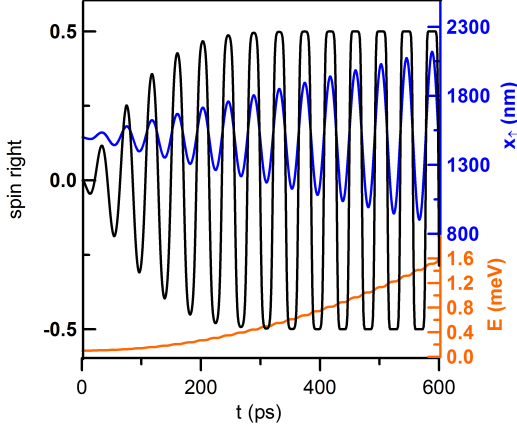


FIG. 7. Time evolution of the spin of the electron trapped in a harmonic potential with sinusoidally varying SOI. Initially the spin is set as an equally weighted linear combination of spin up and down. The blue curve denotes the expectation value of position  $x_{\uparrow}(t)$  calculated for the upper half of the spinor, the red curve—the electron energy, and the black curve—the expectation value of spin  $\sigma_z^R(t)$  in the right half of the quantum wire.

### E. Spin density separation

Now let us assume that the spin of the electron is neither parallel nor antiparallel to the  $z$ -axis, but is a linear combination of both basis vectors (Eq. 3, 4), forming a two-row spinor:

$$\Psi(x, t) = \begin{pmatrix} \psi_{\uparrow}(x, t) \\ \psi_{\downarrow}(x, t) \end{pmatrix}. \quad (9)$$

After the SOI is turned on, the upper and lower parts of the spinor gain opposite momenta; hence, this effect can be used for spatial spin separation.

This time, we initially set up the electron spin as an equally weighted linear combination of spins up and down. Moreover, the electron is trapped in a parabolic potential and we initialize it as the ground state of the harmonic oscillator with an assumption of no SOI ( $E_y = 0$ ); thus, the wavefunction is of the form:

$$\Psi(x, t = 0) = \left(\frac{\beta}{2\pi}\right)^{\frac{1}{4}} \begin{pmatrix} 1 \\ 1 \end{pmatrix} e^{-\beta x^2}. \quad (10)$$

Next, we apply an electric field varying sinusoidally with the frequency tuned to the frequency of the harmonic oscillator (for the chosen harmonic potential). Both parts of the spinor behave in different ways, such as wavefunctions of the electron with spin upwards and downwards (Eq. 3, 4). The center of mass of the entire electron does not move; however, if calculated for each spinor component respectively, they move away in an oscillatory fashion with opposite phases and growing amplitude. In Fig. 7, we see the time evolution of such

a system. The expectation value of position for the spin upwards (blue curve) is calculated using the upper component of the spinor (Eq. 9) as

$$x_{\uparrow}(t) = \frac{\int_0^L x |\psi_{\uparrow}(x, t)|^2 dx}{\int_0^L |\psi_{\uparrow}(x, t)|^2 dx}, \quad (11)$$

with  $L$  being the length of the quantum wire. The oscillations of the center of mass of the electron density with spin downwards  $x_{\downarrow}(t)$  (not presented) are similar, but with a phase shifted by  $\pi$ . The expectation value of the Pauli- $z$  matrix  $\hat{\sigma}_z$  (black curve), calculated in the right half of the quantum wire, is

$$\sigma_z^R(t) = \langle \Psi | \hat{\sigma}_z | \Psi \rangle_R = \int_{L/2}^L (|\psi_{\uparrow}(x, t)|^2 - |\psi_{\downarrow}(x, t)|^2) dx \quad (12)$$

and denoted by *spin right* in the figures.

The expectation position of the upward spin density  $x_{\uparrow}(t)$  oscillates similar to the expectation value of position of the electron from Fig. 6. In the parabolic region of the potential, the amplitude of oscillations grows linearly with time. As the oscillations of spin upwards and downwards wavefunctions are phase-shifted by exactly  $\pi$ , these components separate. Now let us look at the orientation of spin in the right half of the quantum wire  $\sigma_z^R(t)$  (black curve). The amplitude stops growing as it reaches the value 0.5 (or  $-0.5$ ), meaning that the entire spin in the right half is oriented upwards (downwards). For better visualization we can define the spatial  $z$ -spin component density as

$$\rho_{\sigma}(x, t) = \Psi^{\dagger}(x, t) \hat{\sigma}_z \Psi(x, t) = |\psi_{\uparrow}(x, t)|^2 - |\psi_{\downarrow}(x, t)|^2, \quad (13)$$

and compare it with the total electron density defined as

$$\rho(x, t) = \Psi^{\dagger}(x, t) \Psi(x, t) = |\psi_{\uparrow}(x, t)|^2 + |\psi_{\downarrow}(x, t)|^2. \quad (14)$$

Fig. 8 shows a comparison of the spin density (red curve) and the total density (black curve) at the moment of maximal spin separation (spin in the right half reaching  $-0.5$ ). In the left part of the wire the spin density completely covers the total density, meaning that in this region the spin is oriented upwards. Consequently, the right half contains the spin oriented downwards. Now, if we put a potential barrier in the center of the quantum wire, the spin density divides into two spatially separated parts with opposite spins.

We should also notice that, as the amplitude of oscillation of the (spin upward) position  $x_{\uparrow}(t)$  increases, the course of spin in the right half of the wire  $\sigma_z^R(t)$  (black curve in the Fig. 7) starts to form plateaus and resemble a square wave. Therefore, time intervals with separated spins (plateaus) become longer compared to the intervals of spin changes. This increases the tolerance for the moment of the potential barrier creation. Fig. 9 shows the results of a simulation, in which a potential barrier was created in the center of the potential well at about  $t = 500$  ps.



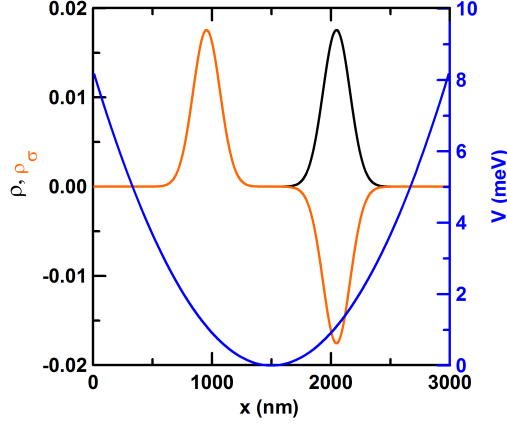


FIG. 8. Comparison of the spatial  $z$ -spin density  $\rho_\sigma(x, t)$  (red curve) with the total spatial density  $\rho(x, t)$  (black curve) at the moment of maximal separation. The spin density divides into two separate parts with opposite spins. Additionally, the confinement potential is shown as a blue curve.

The wavefunction of the electron state shown in Fig. 8 is of Schrödinger's cat type<sup>40,44</sup> and it can be written as  $|\uparrow\rangle|L\rangle + |\downarrow\rangle|R\rangle$  with states  $|\uparrow\rangle$  and  $|\downarrow\rangle$  denoting spin orientations, and states  $|L\rangle$  and  $|R\rangle$  denoting localization of the electron, respectively, in the left and right half of the quantum wire. After separation of both parts of the spin density with a potential barrier, the parts can be relocated to arbitrary positions and the wavefunction still describes the Schrödinger's cat state. Such a wavefunction also has another important feature, that is, it constitutes an entangled state of spin state and state localized in two different spatial regions<sup>40</sup>. This state has

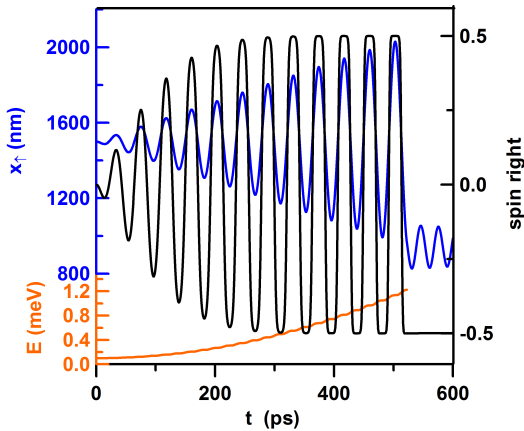


FIG. 9. Simulation of the time evolution of the electron spin (as in Fig. 7), but with the creation of a potential barrier at about  $t = 500$  ps with simultaneous cessation of RSOI oscillations. Markings as in the Fig. 7.

been observed experimentally in ion traps<sup>44,46,52,59</sup>.

The purpose of our study is to design a nanodevice based on a planar semiconductor heterostructure in which this effect could be observed. In simulations presented in Figs. 2-6, we have shown movement of the electron as a whole. In this case, self-focusing was beneficial, since it stabilized the shape of the wavepacket. Its influence was calculated with the image charge method under the assumption that distance  $d$  between the quantum wire and the metallic electrode was equal to 50 nm. In subsequent simulations (Figs. 7-9), self-focusing had to be eliminated, because during separation both spin parts interact with each other through the induced charge which, as a result, destroys the parabolicity of the confinement potential and changes the frequency of oscillations. The self-focusing was mitigated by placing the quantum wire at a greater distance from the electrode (we assumed  $d = 1000$  nm). During the design stage of a real nanodevice we cannot proceed this way and self-focusing has to be compensated in a different manner.

### III. NANODEVICE GENERATING SCHRÖDINGER'S CAT STATES

#### A. Nanodevice design and principles of simulation

For practical realization of the nanodevice we propose a typical planar semiconductor heterostructure with a quantum well (QW) parallel to its surface. The Fig. 10 shows a schematic view of the proposed nanodevice. The

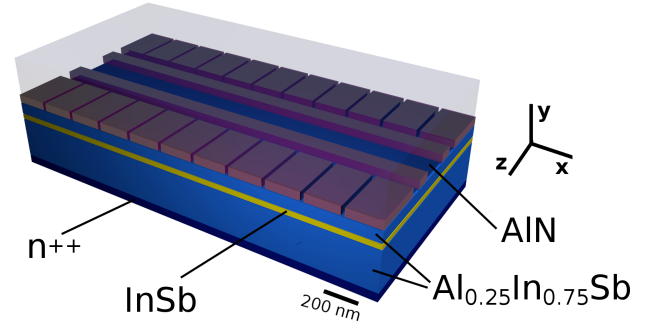


FIG. 10. Schematic view of the proposed nanodevice. The top electrode is not shown.

QW is made of InSb which has a relatively high Rashba coupling. Two blocking layers, below and above the QW, are made of  $\text{Al}_x\text{In}_{1-x}\text{Sb}$  ternary with  $x = 25\%$ , for which the bottom of the conduction band is shifted upwards by 320 meV, creating potential barriers<sup>60–62</sup>. The substrate may consist of  $\text{Al}_x\text{In}_{1-x}\text{Sb}$  highly doped with donors ( $n^{++}$ ). The lower blocking layer is 230 nm thick, while the upper one is of a thickness of 50 nm. The InSb QW inbetween is 20 nm thick. An array of electrodes, as depicted in Fig. 11 ( $y_0$  denotes the  $y$ -position of the QW), is deposited on the heterostructure. Moreover, the

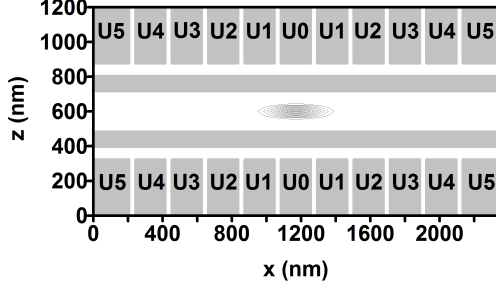


FIG. 11. The layout of the electrode array viewed from above, and the density of the trapped electron, localized at the initial moment in the center, calculated as  $|\Psi(x, z, t = 0)|^2$ .

top of the structure is covered with a layer of dielectric material (AlN) of thickness 320 nm. Finally, we put an additional layer of metal on the dielectric (not shown in the picture).

If there is no electric field, the electrons fill the QW until the Fermi level, creating a two dimensional electron gas (2DEG). Electrons trapped in the QW have two degrees of freedom in lateral directions ( $x$  and  $z$ ). By applying negative voltages to electrodes (in relation to the substrate) we can remove the 2DEG from the quantum well leaving only one electron trapped between two long central electrodes (rails). The voltages applied to the rails block electron movement along the  $z$ -axis. To the remaining electrodes, we apply voltages creating a parabolic confinement potential along the  $x$ -axis.

The potential distribution in the nanodevice is calculated by solving the Poisson's equation in a computational box surrounding the entire device. To simplify the boundary conditions setup, we covered the entire structure with a layer of metal, although it does not have any considerable impact on the operation of the nanodevice. We have chosen a computational box with dimensions  $L_x = 2340$  nm,  $L_z = 1200$  nm,  $L_y = 620$  nm as optimal. In the simulations we consider all the complexity of the structure by including the geometry details, voltages applied to the substrate and electrodes, the time dependent distribution of the electron in the QW, and also the charge induced on the electrodes or the (conducting) substrate.

The confined electron is treated as a particle in a 2D QW; hence, we assume a time dependent Hamiltonian of the form:

$$H(x, z, t) = \left( -\frac{\hbar^2}{2m} (\partial_x^2 + \partial_z^2) - |e|\varphi_{\text{conf}}(x, z, y_0, t) \right) 1_2 + H_R(x, z, y_0, t). \quad (15)$$

Here  $m = 0.014m_e$  denotes the effective mass of an electron in InSb material, and  $\varphi_{\text{conf}}$  constitutes the potential felt by the electron calculated as

$$\varphi_{\text{conf}}(\mathbf{r}, t) = \varphi_{\text{tot}}(\mathbf{r}, t) - \varphi_{\text{self}}(\mathbf{r}, t), \quad (16)$$

with  $\varphi_{\text{tot}}$  being the total potential inside the nanodevice calculated at each time step using the generalized Poisson's equation

$$\nabla \cdot [\epsilon_0 \epsilon(\mathbf{r}) \nabla \varphi_{\text{tot}}(\mathbf{r}, t)] = -\rho(\mathbf{r}, t). \quad (17)$$

This is solved with boundary conditions created by voltages applied to the electrodes. The charge distribution  $\rho(\mathbf{r}, t)$  is calculated as in (Eq. 14), but here in three dimensions. We also need to subtract the Coulomb potential, originating directly from the electron distribution, from the total potential to avoid electron self-interaction. This is calculated as

$$\varphi_{\text{self}}(\mathbf{r}, t) = \frac{-|e|}{4\pi\epsilon\epsilon_0} \int d^3\mathbf{r}' \frac{\rho(\mathbf{r}, \mathbf{t}')}{|\mathbf{r} - \mathbf{r}'|}. \quad (18)$$

Details of this method can be found in [23]. The last term of (Eq. 15) constitutes the RSOI given by the following Hamiltonian:

$$H_R(\mathbf{r}, t) = -\frac{\alpha_{\text{so}}|e|}{\hbar} [\nabla \varphi_{\text{conf}}(\mathbf{r}, t) \times \hat{\mathbf{p}}] \cdot \hat{\boldsymbol{\sigma}}, \quad (19)$$

with the Rashba coupling  $\alpha_{\text{so}} = 523 \text{ \AA}^2$  for InSb material<sup>29</sup>.

We apply voltages to the electrode array depicted in the Fig. 11. Initially the rails and the top electrode are set to  $U = -400$  mV. To the side electrodes located in the center of the structure (electrodes  $U_0$ ) we apply voltages 10 mV lower ( $U_0 = U - 10 \text{ mV} = -410$  mV). Voltages for the remaining side electrodes are calculated as  $U_i = U_0 - \gamma i^2$  with  $\gamma = 5$  mV.

Now, we generate the ground state of an electron using the imaginary time evolution method<sup>63</sup>. Then, during the real time evolution of the system we change sinusoidally the voltages applied to the electrodes, according to the formula

$$U(t) = \tilde{U} + \Delta\tilde{U} \sin(\omega t), \quad (20)$$

with  $\tilde{U} = -400$  mV,  $\Delta\tilde{U} = 300$  mV and  $\omega$  tuned to the characteristic frequency of the obtained harmonic confinement potential. Voltages applied to the remaining electrodes are shifted in relation to the  $U(t)$  voltage in the same way as at the beginning of the simulation. Consequently, the shape of the confinement potential along the  $x$ -axis remains virtually the same (parabolic with the same curvature) for the entire simulation, even though the potential is shifted by a time dependent value. Oscillations of voltages cause oscillations of the electric field perpendicular to the surface of the nanostructure and thereby the SOI oscillates as well.

## B. Preliminary simulations

Since the simulation within the 1D model has shown that self-focusing destroys the potential parabolicity, the first 3D simulations were performed without this effect.

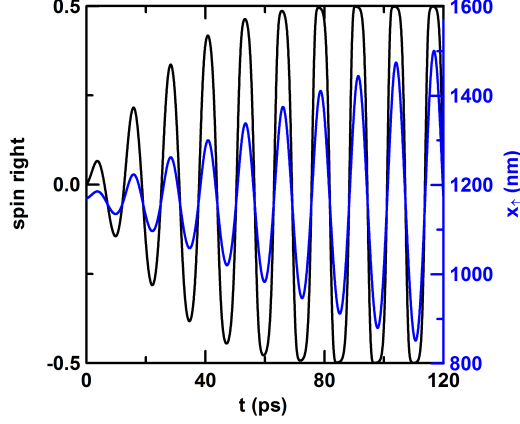


FIG. 12. Simulation of the time evolution for the electron trapped in the nanodevice presented in the Figs. 10 and 11 with sinusoidally varying voltages applied to the electrodes. Initially the electron spin is oriented along the  $x$ -axis. The blue curve shows the position calculated for the upper spinor part  $x_+(t)$  and the black one denotes the  $z$ -spin component calculated in the right half of the potential well  $\sigma_z^R(t)$ . This simulation neglects the self-focusing effect.

This can be easily done by neglecting the presence of charge in the Poisson's equation. In Fig. 12, we see results of such a simulation obtained for a frequency of oscillations (Eq. 20) corresponding to the harmonic oscillator energy  $\hbar\omega = 0.331$  meV.

We start from the electron wavefunction with spin oriented along the  $x$ -axis, i.e. an equally weighted linear combination of spin up and down components, generated as the ground state of the parabolic confinement potential. We perform simulations with correctly tuned voltage oscillation frequency (in Eq. 20). As a result, we get expectation values of spin in the right half of the nanodevice (black curve) similar to the time courses from Fig. 7. The curve reaches the value  $\sigma_z^R(t) > 0.499$ , which indicates almost full spatial spin separation. The long plateau regions with  $\sigma_z^R(t) \approx 0.5$  mean that the intervals in which the spin remains separated are long enough to set an additional potential barrier between the separated spin density parts to further enhance separation.

In Fig. 13, we can see another case of such simulations, but this time with the self-focusing effect included. The Poisson's equation is solved with the same permittivity (InSb)  $\epsilon = 17.9$  for the entire computational box. This corresponds to a hypothetical situation in which the nanostructure is covered not with a dielectric layer but with a semiconductor layer of permittivity similar to the InSb. This time the wavefunctions with opposite spins do not fully separate and  $\sigma_z^R(t)$  does not reach the value of 0.5 (or  $-0.5$ ) closely enough. The Poisson's equation solution includes the self-focusing effect caused by the induced charge in both, the electrodes and the conducting substrate. The sources of this charge have an influence

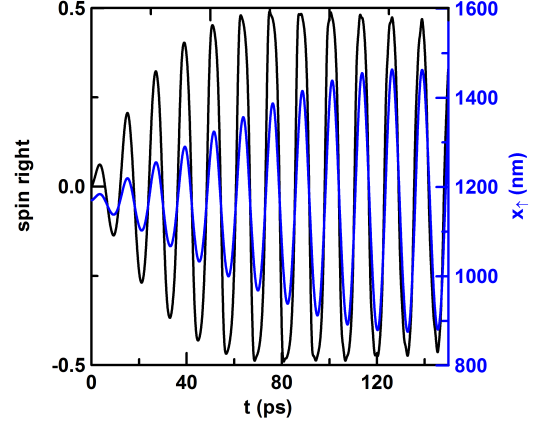


FIG. 13. Simulation similar to that from Fig. 12 but with self-focusing effect included and the permittivity value for InSb ( $\epsilon = 17.9$ ) set for the entire computational box. The markings are as in Fig. 12.

on the potential felt by the electron.

Let us look at Fig. 14. It presents how the potential energy in the QW changes with the inclusion of the self-focusing effect. The case with self-focusing (blue curve) clearly deviates from the case without self-focusing (red curve). The potential energy for the first case (blue curve) remains acceptably parabolic, but during wavefunction separation, the interaction with the induced charge weakens, since the wavepacket splits into two separated parts and the potential felt by each one changes. These changes and the resulting non-parabolicity hinder the electron acceleration. The effect of self-focusing could

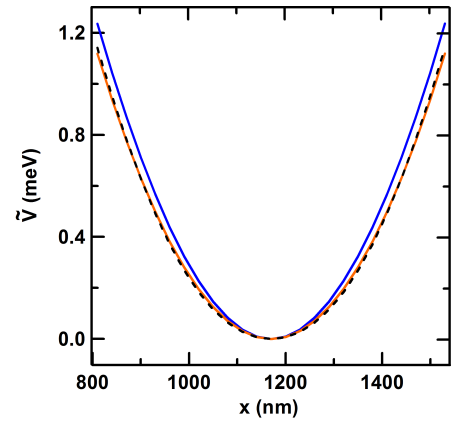


FIG. 14. Potential energies in the vicinity of their minima, calculated for three cases: (red curve) with self-focusing neglected, (blue curve) with self-focusing taken into account, and (black dashed curve) with self-focusing included for a nanostructure covered with a dielectric layer. All potentials are shifted, so that the minima coincide.



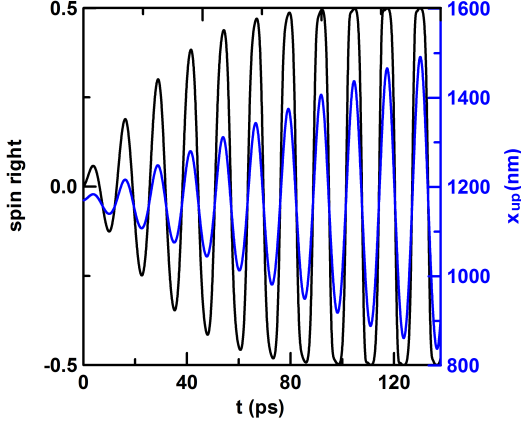


FIG. 15. Simulation of the time evolution of the electron trapped in the nanostructure with dielectric compensation of self-focusing. Markings as in Fig. 12.

be mitigated by increasing the distance between the QW and the electrodes or the substrate.

### C. Effect of adding a dielectric

In the proposed nanostructure (Fig. 10), the distance between the QW and the substrate is 240 nm and for the top metallic electrode 380 nm, which are high enough for negligible self-focusing. However, to neutralize the influence of self-focusing originating from the rails and the side electrodes, we employ another nanodevice design. This is achieved by placing a dielectric layer on top of these electrodes—see Fig. 10 (but under the top electrode), with permittivity lower than the permittivity of the QW material. For this purpose, we used AlN material with permittivity  $\epsilon = 7.6$ . If we used the image charge method for the interface of two dielectric media, the image charge induced within the material of lower permittivity would have the same sign as the primary charge (located in the material of higher permittivity). Therefore, such a dielectric addition could compensate the charge induced on metallic electrodes. We observe such an effect in simulations. In Fig. 14, the black dashed curve shows the potential energy calculated for one such case of compensation. In the device region between 800 nm and 1500 nm in which the electron is accelerated and separated ( $x_{\uparrow}(t)$  oscillations range—see: Fig. 13), the black curve from Fig. 14 coincides with the red one. This clearly means that self-focusing has been neutralized by defocusing due to the presence of the dielectric layer. Such a compensation also requires a careful tuning of the rail widths and the distance between them. Fig. 11 shows relatively large areas not covered with any electrodes. In these areas the semiconductor comes into direct contact with the dielectric.

Fig. 15 shows results of the simulation with spin-

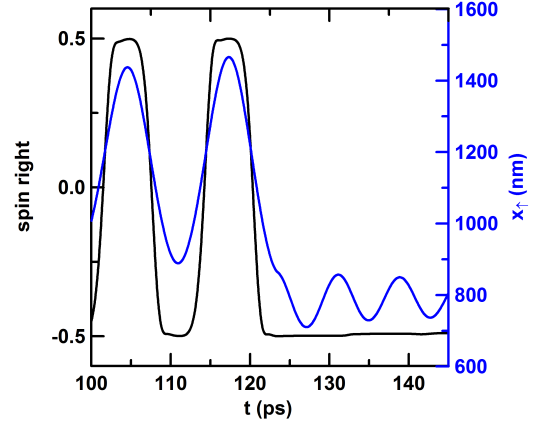


FIG. 16. Fragment of the time evolution with visible results of setting up the barrier, dividing the nanodevice into two regions. Markings as in Fig. 12.

dependent electron acceleration due to oscillating spin-orbit coupling in the nanostructure covered with the dielectric layer. This time the tuned voltage oscillation frequency is of  $\hbar\omega = 0.325$  meV. The course of the expectation value of  $\sigma_z^R(t)$  starts to resemble ones from Figs. 7 and 12. Characteristic plateaus appear again, giving a lot of time for setting up a potential barrier between the separated parts. The most favorable moment to create such a barrier is at  $t_1 = 123$  ps. At this moment we stop any oscillations of voltages and keep them fixed. Moreover, for the two electrodes marked as  $U_0$  the voltages are decreased by 150 mV, namely  $U_0(t_1) = U(t_1) - 160$  mV. This procedure elevates the potential in the center of the structure, creating a potential barrier. This effectively divides the nanodevice into two regions: left and right. The last fragment of the simulation depicting the barrier setup moment is shown in Fig. 16. The  $\sigma_z^R(t)$  (black curve) remains close to the value  $-0.5$ , which means that spin in the right part of the nanodevice is oriented downwards. The spin upwards position  $x_{\uparrow}(t)$  (blue curve) no longer returns to the upper part of the graph but it falls and remains down due to the repulsive influence of the barrier.

Now, the  $x_{\uparrow}(t)$  starts to oscillate in the left half of the nanodevice. These oscillations indicate that, during the separation stage, the electron did not get rid of the excess of energy. The frequency of the oscillations has also changed, since the local curvature of the confinement potential is now slightly different. The oscillations have a negative influence on the working of the nanodevice, because the separated spin density part can tunnel through the barrier while returning to it. This manifests itself via a small rise in the final part of the  $\sigma_z^R(t)$  course (barely visible in Fig. 16). Oscillations, however, can be easily eliminated by subsequent elevation of the barrier at the moment when the velocity of spin density parts (i.e.  $\frac{d}{dt}x_{\uparrow}(t)$  and  $\frac{d}{dt}x_{\downarrow}(t)$ ) is zero. Fig. 16 shows

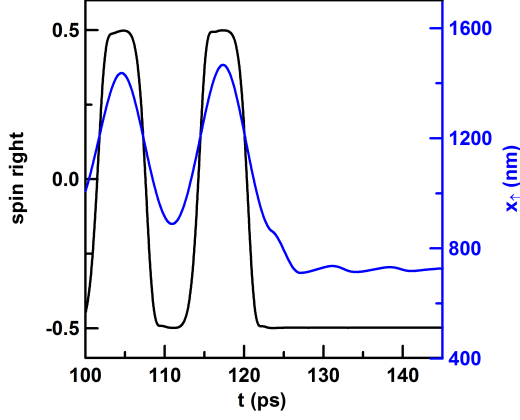


FIG. 17. The final fragment of the time evolution of the system with the potential barrier setup and its subsequent elevation. Markings as in Fig. 12.

a good candidate for such a moment at  $t_2 = 127$  ps. The barrier is elevated by decreasing the voltage applied to the  $U_0$  electrode by an additional 100 mV (now  $U_0(t_2) = U(t_1) - 260$  mV). Fig. 17 shows results of a simulation for that case. Fig. 18 shows the wavepacket and the potential barrier in the nanodevice center at the moment of maximal separation. This time we compare the spin and total electron densities calculated along the  $x$ -axis but, unlike the 1D case, here also integrated along the  $z$  direction. We use the following formulae:

$$\begin{aligned} \rho_\sigma(x, t) &= \int_0^{L_z} dz \Psi^\dagger(x, z, t) \hat{\sigma}_z \Psi(x, z, t) \\ &= \int_0^{L_z} dz (|\psi_\uparrow(x, z, t)|^2 - |\psi_\downarrow(x, z, t)|^2), \end{aligned} \quad (21)$$

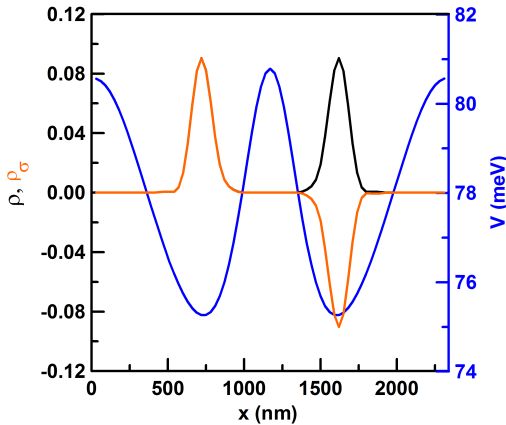


FIG. 18. Final shapes of: (red curve) the spin density divided into two spatially separated parts with opposite spins, (black curve) the total density, and (blue curve) the confinement potential at  $z_0 = L_z/2$ . The densities are defined according to (Eq. 21, 22).

$$\begin{aligned} \rho(x, t) &= \int_0^{L_z} dz \Psi^\dagger(x, z, t) \Psi(x, z, t) \\ &= \int_0^{L_z} dz (|\psi_\uparrow(x, z, t)|^2 + |\psi_\downarrow(x, z, t)|^2), \end{aligned} \quad (22)$$

The potential energy has two minima with a barrier between them. Both parts of the spin density are separated and oscillate closely around these minima, but the amplitude of oscillation is much smaller than in the case in which the potential barrier was elevated only once. If we raise a barrier of full height at the first time by lowering the voltages by the full 250 mV at time  $t_1$ , the amplitude of the oscillations will be significantly higher.

#### IV. SUMMARY

We proposed a design for a nanodevice based on a typical planar semiconductor heterostructure in which it is possible to create an entangled state of Schrödinger's cat type. This is achieved by spatial separation of the electron densities corresponding to opposite spin directions. Such a state has been generated in quantum optics<sup>44–46</sup>.

To create this state in our nanostructure, we need to use coherent states of the harmonic oscillator which are obtainable only for ideally parabolic confinement potentials. Generation of such a potential is one of the most important results of this paper. Nearly ideal parabolic potential along the  $x$ -axis is achievable in the proposed multi-electrode nanodevice (see: Figs. 10 and 11) if we neglect the interaction of the electron confined in the quantum well with the induced charge on the device electrodes. This interaction causes self-focusing of the electron density, making spin separation much harder. A remedy for this effect is defocusing achieved by covering the entire nanostructure with a dielectric of lower permittivity compared to the well material. We have shown that self-focusing can be effectively compensated by adding a dielectric layer with simultaneous careful adjustment of the inner electrode (rails) geometry.

We have performed simulations of numerous variants of our nanodevice via solution of the time dependent Schrödinger equation with simultaneous tracking of the potential via solution of the Poisson's equation at every time step. As a result, we were able to take into account the geometry details, varying voltages applied to electrodes and changes of the electron density. Including also oscillating spin-orbit interaction, which induces the spin separation effect.

#### ACKNOWLEDGMENTS

This work has been supported by National Science Centre, Poland, under UMO-2014/13/B/ST3/04526.

- <sup>1</sup> R. Hanson, L. P. Kouwenhoven, J. R. Petta, S. Tarucha, and L. M. K. Vandersypen, *Rev. Mod. Phys.* **79**, 1217 (2007).
- <sup>2</sup> I. Žutić, J. Fabian, and S. Das Sarma, *Rev. Mod. Phys.* **76**, 323 (2004).
- <sup>3</sup> T. D. Ladd, F. Jelezko, R. Laflamme, Y. Nakamura, C. Monroe, and J. L. O'Brien, *Nature* **464**, 45 (2010).
- <sup>4</sup> M. Z. Hasan and C. L. Kane, *Rev. Mod. Phys.* **82**, 3045 (2010).
- <sup>5</sup> P. Zhang and F. Nori, *Phys. Rev. B* **92**, 115303 (2015).
- <sup>6</sup> L. Fu and C. L. Kane, *Phys. Rev. Lett.* **100**, 096407 (2008).
- <sup>7</sup> R. M. Lutchyn, J. D. Sau, and S. Das Sarma, *Phys. Rev. Lett.* **105**, 077001 (2010).
- <sup>8</sup> J. Klinovaja, P. Stano, and D. Loss, *Phys. Rev. Lett.* **109**, 236801 (2012).
- <sup>9</sup> Y. Oreg, G. Refael, and F. von Oppen, *Phys. Rev. Lett.* **105**, 177002 (2010).
- <sup>10</sup> E. T. Owen, M. C. Dean, and C. H. W. Barnes, *Phys. Rev. A* **89**, 032305 (2014).
- <sup>11</sup> A. Bertoni, P. Bordone, R. Brunetti, C. Jacoboni, and S. Reggiani, *Phys. Rev. Lett.* **84**, 5912 (2000).
- <sup>12</sup> T. Hayashi, T. Fujisawa, H. D. Cheong, Y. H. Jeong, and Y. Hirayama, *Phys. Rev. Lett.* **91**, 226804 (2003).
- <sup>13</sup> K. D. Petersson, J. R. Petta, H. Lu, and A. C. Gossard, *Phys. Rev. Lett.* **105**, 246804 (2010).
- <sup>14</sup> D. Loss and D. P. DiVincenzo, *Phys. Rev. A* **57**, 120 (1998).
- <sup>15</sup> C. Kloeffer and D. Loss, *Annu. Rev. Condens. Matter Phys.* **4**, 51 (2013).
- <sup>16</sup> M. D. Shulman, O. E. Dial, S. P. Harvey, H. Bluhm, V. Umansky, and A. Yacoby, *Science* **336**, 202 (2012).
- <sup>17</sup> L. Trifunovic, O. Dial, M. Trif, J. R. Wootton, R. Abebe, A. Yacoby, and D. Loss, *Phys. Rev. X* **2**, 011006 (2012).
- <sup>18</sup> L. Trifunovic, F. L. Pedrocchi, and D. Loss, *Phys. Rev. X* **3**, 041023 (2013).
- <sup>19</sup> A. Pal, E. I. Rashba, and B. I. Halperin, *Phys. Rev. B* **92**, 125409 (2015).
- <sup>20</sup> S. Mehl and D. P. DiVincenzo, *Phys. Rev. B* **92**, 115448 (2015).
- <sup>21</sup> F. Hassler, G. Catelani, and H. Bluhm, *Phys. Rev. B* **92**, 235401 (2015).
- <sup>22</sup> P. Szumniak, J. Pawłowski, S. Bednarek, and D. Loss, *Phys. Rev. B* **92**, 035403 (2015).
- <sup>23</sup> S. Bednarek, B. Szafran, R. J. Dudek, and K. Lis, *Phys. Rev. Lett.* **100**, 126805 (2008).
- <sup>24</sup> S. Bednarek and B. Szafran, *Nanotechnology* **20**, 065402 (2009).
- <sup>25</sup> S. Bednarek, P. Szumniak, and B. Szafran, *Phys. Rev. B* **82**, 235319 (2010).
- <sup>26</sup> S. Bednarek and B. Szafran, *Phys. Rev. Lett.* **101**, 216805 (2008).
- <sup>27</sup> E. Rashba, *Sov. Phys. Solid State* **2**, 1109 (1960).
- <sup>28</sup> Y. A. Bychkov and E. I. Rashba, *Journal of Physics C: Solid State Physics* **17**, 6039 (1984).
- <sup>29</sup> R. Winkler, *Spin-orbit Coupling Effects in Two-Dimensional Electron and Hole Systems* (Springer-Verlag Berlin Heidelberg, 2003).
- <sup>30</sup> K. C. Nowack, F. H. L. Koppens, Y. V. Nazarov, and L. M. K. Vandersypen, *Science* **318**, 1430 (2007).
- <sup>31</sup> S. Nadj-Perge, S. Frolov, E. Bakkers, and L. P. Kouwenhoven, *Nature* **468**, 1084 (2010).
- <sup>32</sup> S. Nadj-Perge, V. S. Pribiag, J. W. G. van den Berg, K. Zuo, S. R. Plissard, E. P. A. M. Bakkers, S. M. Frolov, and L. P. Kouwenhoven, *Phys. Rev. Lett.* **108**, 166801 (2012).
- <sup>33</sup> M. Malard, I. Grusha, G. I. Japaridze, and H. Johanneson, *Phys. Rev. B* **84**, 075466 (2011).
- <sup>34</sup> A. López, Z. Z. Sun, and J. Schliemann, *Phys. Rev. B* **85**, 205428 (2012).
- <sup>35</sup> Y. Ban, X. Chen, E. Y. Sherman, and J. G. Muga, *Phys. Rev. Lett.* **109**, 206602 (2012).
- <sup>36</sup> T. Čadež, J. H. Jefferson, and A. Ramšak, *Phys. Rev. Lett.* **112**, 150402 (2014).
- <sup>37</sup> V. Szaszko-Bogár, F. M. Peeters, and P. Földi, *Phys. Rev. B* **91**, 235311 (2015).
- <sup>38</sup> J. Pawłowski, P. Szumniak, and S. Bednarek, *Phys. Rev. B* **93**, 045309 (2016).
- <sup>39</sup> J. Pawowski, P. Szumniak, A. Skubis, and S. Bednarek, *Journal of Physics: Condensed Matter* **26**, 345302 (2014).
- <sup>40</sup> D. J. Wineland, *Rev. Mod. Phys.* **85**, 1103 (2013).
- <sup>41</sup> H. W. Lau, Z. Dutton, T. Wang, and C. Simon, *Phys. Rev. Lett.* **113**, 090401 (2014).
- <sup>42</sup> T. C. Ralph, A. Gilchrist, G. J. Milburn, W. J. Munro, and S. Glancy, *Phys. Rev. A* **68**, 042319 (2003).
- <sup>43</sup> J.-Q. Liao, J.-F. Huang, and L. Tian, *Phys. Rev. A* **93**, 033853 (2016).
- <sup>44</sup> C. Monroe, D. M. Meekhof, B. E. King, and D. J. Wineland, *Science* **272**, 1131 (1996).
- <sup>45</sup> D. Leibfried, R. Blatt, C. Monroe, and D. Wineland, *Rev. Mod. Phys.* **75**, 281 (2003).
- <sup>46</sup> C. J. Myatt, B. E. King, Q. A. Turchette, C. A. Sackett, D. Kielpinski, W. M. Itano, C. Monroe, and D. J. Wineland, *Nature* **403**, 269 (2000).
- <sup>47</sup> C. Sackett, D. Kielpinski, B. King, C. Langer, V. Meyer, C. Myatt, M. Rowe, Q. Turchette, W. Itano, D. Wineland, *et al.*, *Nature* **404**, 256 (2000).
- <sup>48</sup> H. Jeong and M. S. Kim, *Phys. Rev. A* **65**, 042305 (2002).
- <sup>49</sup> E. T. Owen, M. C. Dean, and C. H. W. Barnes, *Phys. Rev. A* **85**, 022319 (2012).
- <sup>50</sup> J. Pawłowski, P. Szumniak, and S. Bednarek, *arXiv preprint arXiv:1602.08531* (2016).
- <sup>51</sup> R. Blatt and D. Wineland, *Nature* **453**, 1008 (2008).
- <sup>52</sup> M. J. McDonnell, J. P. Home, D. M. Lucas, G. Imreh, B. C. Keitch, D. J. Szwer, N. R. Thomas, S. C. Webster, D. N. Stacey, and A. M. Steane, *Phys. Rev. Lett.* **98**, 063603 (2007).
- <sup>53</sup> S. Bednarek and B. Szafran, *Phys. Rev. B* **73**, 155318 (2006).
- <sup>54</sup> S. Bednarek, B. Szafran, and K. Lis, *Phys. Rev. B* **72**, 075319 (2005).
- <sup>55</sup> P. Szumniak, S. Bednarek, B. Partoens, and F. M. Peeters, *Phys. Rev. Lett.* **109**, 107201 (2012).
- <sup>56</sup> S. Bednarek, K. Lis, and B. Szafran, *Phys. Rev. B* **77**, 115320 (2008).
- <sup>57</sup> C. Zener, in *Proceedings of the Royal Society of London A: Mathematical, Physical and Engineering Sciences*, Vol. 137 (The Royal Society, 1932) pp. 696–702.
- <sup>58</sup> T. Kato, *Journal of the Physical Society of Japan* **5**, 435 (1950).
- <sup>59</sup> Q. A. Turchette, C. J. Myatt, B. E. King, C. A. Sackett, D. Kielpinski, W. M. Itano, C. Monroe, and D. J. Wineland, *Phys. Rev. A* **62**, 053807 (2000).

- <sup>60</sup> N. Dai, G. A. Khodaparast, F. Brown, R. E. Doezema, S. J. Chung, and M. B. Santos, Applied Physics Letters **76** (2000).
- <sup>61</sup> N. Dai, F. Brown, R. E. Doezema, S. J. Chung, K. J. Goldammer, and M. B. Santos, Applied Physics Letters **73** (1998).
- <sup>62</sup> F. Gouider, Y. B. Vasilyev, M. Bugár, J. Könemann, P. D. Buckle, and G. Nachtwei, Phys. Rev. B **81**, 155304 (2010).
- <sup>63</sup> K. Davies, H. Flocard, S. Krieger, and M. Weiss, Nuclear Physics A **342**, 111 (1980).